Journal of Systems Engineering and Electronics
Vol. 35, No. 4, August 2024, pp.874 – 887

Novel method for extraction of ship target with overlaps in SAR image via EM algorithm

CAO Rui and WANG Yong*

School of Electronics and Information Engineering, Harbin Institute of Technology, Harbin 150001, China

Abstract: The quality of synthetic aperture radar (SAR) image degrades in the case of multiple imaging projection planes (IPPs) and multiple overlapping ship targets, and then the performance of target classification and recognition can be influenced. For addressing this issue, a method for extracting ship targets with overlaps via the expectation maximization (EM) algorithm is proposed. First, the scatterers of ship targets are obtained via the target detection technique. Then, the EM algorithm is applied to extract the scatterers of a single ship target with a single IPP. Afterwards, a novel image amplitude estimation approach is proposed, with which the radar image of a single target with a single IPP can be generated. The proposed method can accomplish IPP selection and targets separation in the image domain, which can improve the image quality and reserve the target information most possibly. Results of simulated and real measured data demonstrate the effectiveness of the proposed method.

Keywords: expectation maximization (EM) algorithm, image processing, imaging projection plane (IPP), overlapping ship target, synthetic aperture radar (SAR).

DOI: 10.23919/JSEE.2023.000170

1. Introduction

Radar imaging for ship target is important for maritime surveillance [1−4]. However, two special circumstances in the synthetic aperture radar (SAR) imaging are disadvantageous for the target classification and recognition. One is the multiple imaging projection planes (IPPs), the other is overlapping multiple targets. Hence, it is important for achieving IPP selection and target separation.

In the first case, the IPP is changing within the imaging interval, which is aroused by the complex motion of maritime targets [5−7]. For this reason, the SAR image obtained by the conventional algorithm shows multiple attitudes of ship targets. For improving the image quality and better extracting target feature, multiple IPPs should be restricted as the single IPP firstly [8−11]. Generally, the common solution is to select the optimal time interval, and many effective methods are proposed for decades. In [12,13], Pastina et al. achieved the IPP selection combined with the angular motion parameters estimation technique. In [14−18], several optimal time selection methods were presented with measuring the stationarity of Doppler frequency. These methods can obtain the single IPP, however two main issues are involved: (i) the image sequence usually needs to be generated, which consumes large computational complexity; (ii) the SAR image needs to be inverse-mapped into the echo domain.

In the second case, the multiple ship targets are overlapped in the SAR image owing to the close range and azimuth positions [19]. Similar with the first case, the time interval is selected to solve this problem, in which only the single target is illuminated. This operation has three defects: (i) the echo information is wasted; (ii) the image resolution is degraded; (iii) the completeness of the target may be broken.

Great challenges are presented by these two special cases, especially for the imaging quality, target classification and recognition. In this paper, this problem is solved with scatterer classification and amplitude estimation from a novel perspective, which is different with conventional time window selection methods in [12−18]. First, the scatterers of the ship target should be well extracted from the SAR image. In this paper, the target detection technique in [5,20] and the OTSU technique in [21] are employed to avoid the influence of background noise, clutter and high sidelobe. Then, a method for extracting the ship target with overlaps is proposed, which can achieve the IPP selection and target separation. The proposed method is composed of the expectation maximization (EM) algorithm and the amplitude estimation method. The EM algorithm is applicable to the overlapping scatterers, with which the scatterers of the single IPP

Manuscript received January 11, 2023.
*Corresponding author.
This work was supported by the National Science Fund for Distinguished Young Scholars (62325104).

and single target can be well extracted. The amplitude estimation method is proposed for recovering the amplitude of these scatterers, which ensures the image quality, the resolution and the completeness of ship targets.

As mentioned above, the classification of scatterers impacts on the performance of ship extraction. Especially for the overlapping scatterer, it should be considered as belonging to multiple clusters, instead of a single cluster. Obviously, the classical clustering algorithms such as k-means algorithm [21−23], hierarchical clustering algorithm [24,25] are inadequate in this case. Therefore, in this paper, the EM algorithm is adopted for the superior classification of overlapping scatterers since it can calculate the probability that each pixel belongs to each cluster [26,27].

The rest content is arranged as follows. Firstly, the SAR processing method and data preprocessing technique are introduced in Section 2, and then the problem to be solved is described as the estimation of two dimensional (2D) Gaussian mixture model (GMM). Afterwards, the proposed method is elaborated in Section 3, involving the EM algorithm and amplitude estimation method. Subsequently, the availability of the proposed method is validated by results of simulated and real measured data in Section 4. Finally, the conclusions are drawn in Section 5.

2. SAR processing algorithm, data preprocessing technique, and mathematical model establishment

In this section, the chirp scaling (CS) algorithm in [28] is introduced firstly for SAR processing. Afterwards, the data preprocessing technique is elaborated integrally, which combines the target detection method in [20] and the OTSU method in [21]. Afterwards, the phenomena of multiple IPPs and overlapping targets is interpreted with the mathematical model, after that the problem to be solved is described as the estimation of GMM.

2.1 SAR processing algorithm

In this paper, the CS algorithm in [28] is applied for the SAR imaging. First, the CS algorithm compensates the range curvatures in the different range positions. Then, the residual range migration is compensated. Afterwards, the residual phase compensation is accomplished after the range compression. Finally, the SAR image can be obtained with the azimuth compression, denoted as $I_O(m,n)$. Here, m and n are the azimuth and range position, respectively, $m=1,2,\cdots,N_a$, $n=1,2,\cdots,N_r$, and N_a and N_r are the numbers of azimuth and range bins, respectively.

Then, the EM algorithm can be implemented to extract the multiple target attitudes or separate the overlapping targets. Nevertheless, one precondition needs to be satisfied that the potential scatterers of the target should be well extracted from the SAR image, and the undesirable samples arose from background noise, clutter and high sidelobe should be ignored. For this purpose, the target detection technique in [20] and the OTSU method in [21] are adopted. The integrated procedure will be elaborated in the next part.

2.2 Data preprocessing technique

It is assumed that there are K IPPs or K overlapping ship targets in the SAR image. Generally, the integrated procedure includes the following steps [20,21].

Step 1 Prescreening technique

A 2D window is designed to detect the potential samples of the ship target. The window is composed of the background area, the guarding area and the sample under detection (SUD), as summarized in Fig. 1. The amplitude ratio between the SUD and the average background noise is used to detect the potential samples.

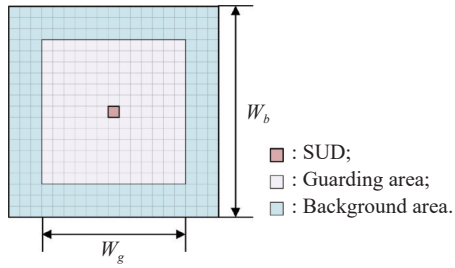

Fig. 1 Structure of 2D window

The background area can be expressed as

$$F(w_m,w_n)=\begin{cases}0, & w_m\in\left[m-\dfrac{W_g-1}{2},m+\dfrac{W_g-1}{2}\right];\\ & w_n\in\left[n-\dfrac{W_g-1}{2},n+\dfrac{W_g-1}{2}\right];\\ & w_m,w_n\in\mathbf{Z}\\ 1, & \text{others}\end{cases}\tag{1}$$

where $W_b>W_g$, both of them are odd numbers, which express the lengths of 2D window and guarding area, respectively.

The amplitude of background noise can be evaluated by the average amplitude of samples in the background area, which can be calculated as

$$I_b(m,n)=\frac{1}{W_b^2-W_g^2}\cdot\sum_{w_m=m-(W_b-1)/2}^{m+(W_b-1)/2}\sum_{w_n=n-(W_b-1)/2}^{n+(W_b-1)/2}I_O(w_m,w_n)F(w_m,w_n)\tag{2}$$

Afterwards, the SAR image after the prescreening

technique can be obtained as

$$I_P(m,n)=\begin{cases} I_O(m,n), & \dfrac{I_O(m,n)}{I_b(m,n)} \geqslant G_p \\ 0, & \text{others} \end{cases} \tag{3}$$

where $I_O(m,n)$ is the amplitude of SUD, and G_p is the threshold.

Step 2 Morphological filtering technique

The morphological filter is employed for eliminating the isolated samples, after which the SAR image is denoted as $I_{\mathrm{MF}}(m,n)$.

Step 3 Labeling technique

The multiple connected samples are labeled as $l(l=1,2,\cdots,L)$ with the rule of 4-connectivity, where L is the number of sets. Subsequently, the 2D sample set $\boldsymbol{S}_l(m,n)$ is composed, whose centre is located in $s_c(l)=[m_l,n_l]^{\mathrm{T}}$.

Step 4 Rejection technique

Some sample sets are rejected with a more severe threshold G_R owing to the small size and low intensity. Here, the intensity of sample set is compared with background noise.

The integrated amplitude of sample set is calculated by

$$I_a(l)=\sum_m\sum_n \boldsymbol{S}_l(m,n). \tag{4}$$

The background area of the lth sample set can be calculated via

$$\tilde{I}_b(w_{m_l},w_{n_l})=I_{\mathrm{MF}}(w_{m_l},w_{n_l})\cdot F(w_{m_l},w_{n_l}). \tag{5}$$

Then, the contrast of the background area can be solved with

$$I_c(l)=\frac{\sqrt{\mathrm{E}\left\{\left[\tilde{I}_b(w_{m_l},w_{n_l})-\mathrm{E}\left\{\tilde{I}_b(w_{m_l},w_{n_l})\right\}\right]^2\right\}}}{\mathrm{E}\left[\tilde{I}_b(w_{m_l},w_{n_l})\right]}. \tag{6}$$

If $I_a(l)/I_c(l)\geqslant G_R$, the lth sample set can be reserved. Otherwise it is rejected.

Step 5 Fusion technique

The fusion technique merges the adjacent sample set and generate the entire target. If the distance between two sample sets is smaller than a threshold, the smaller sample set will be merged into the bigger one. This procedure will be repeated with several times by using more severe thresholds until the number of sample sets stops changing.

Step 6 OTSU technique

It is considered that some undesirable samples with high sidelobe are selected by Step 1, which is hard to eliminate in the above steps. Hence, the OTSU method [21] is employed to eliminate these samples and obtain the final sample set.

The integrated data preprocessing procedure is summarized in Fig. 2.

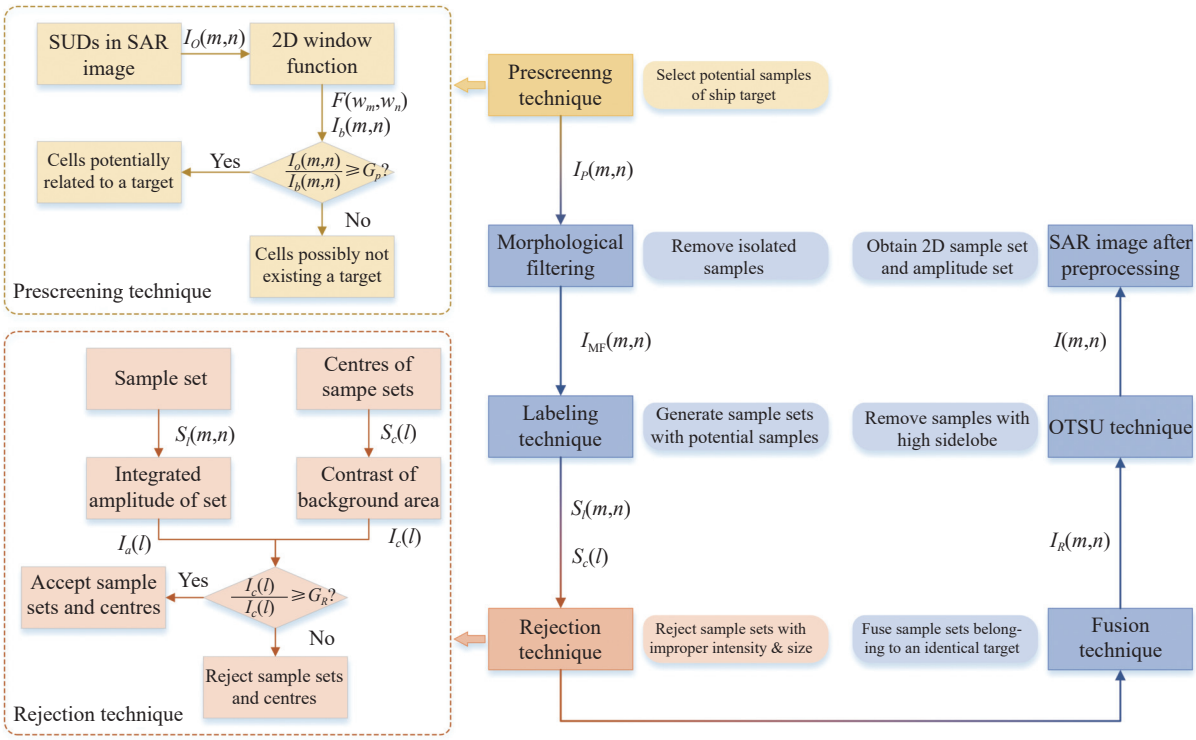

Fig. 2 Flowchart of integrated data preprocessing technique

2.3 GMM

After the data preprocessing technique, the 2D sample set can be acquired and denoted as $S=\{\boldsymbol{s}_1,\boldsymbol{s}_2,\cdots,\boldsymbol{s}_J\}$, and the SAR image is expressed as $I(m,n)$. Here, $\boldsymbol{s}_j=[m_j,n_j]^{\mathrm{T}}$, m_j and n_j are the azimuth and range positions of the jth $(j=1,2,\cdots,J)$ sample and J is the number of samples.

The sample set of S can be classified as K clusters with the clustering analysis. Since the overlapping pixels exist in the SAR image, the 2D GMM is selected for the classification in this paper, where the mean and covariance matrix are denoted as $\boldsymbol{\mu}_k$ and $\boldsymbol{\Sigma}_k$ $(k=1,2,\cdots,K)$, respectively.

Actually, the procedure of classification can be depicted as solving the posterior probability of $P(\boldsymbol{s}_j\in C_k|\boldsymbol{s}_j)$, which can be calculated with Bayes formula [29]:

$$P(\boldsymbol{s}_j\in C_k|\boldsymbol{s}_j)=\frac{P(\boldsymbol{s}_j|\boldsymbol{s}_j\in C_k)P(\boldsymbol{s}_j\in C_k)}{\sum_k P(\boldsymbol{s}_j|\boldsymbol{s}_j\in C_k)P(\boldsymbol{s}_j\in C_k)} \tag{7}$$

where $P(\boldsymbol{s}_j\in C_k)$ represents the prior probability, and $P(\boldsymbol{s}_j|\boldsymbol{s}_j\in C_k)$ is the conditional probability, which can be expressed as

$$P(\boldsymbol{s}_j|\boldsymbol{\mu}_k,\boldsymbol{\Sigma}_k)=(2\pi)^{-\frac{D}{2}}|\boldsymbol{\Sigma}_k|^{-\frac{1}{2}}\exp\left[-\frac{1}{2}(\boldsymbol{s}_j-\boldsymbol{\mu}_k)^{\mathrm{T}}\boldsymbol{\Sigma}_k^{-1}(\boldsymbol{s}_j-\boldsymbol{\mu}_k)\right] \tag{8}$$

and $D=2$ in this paper.

The optimal GMM for the sample set S can be described as

$$p(S;\boldsymbol{\Theta}^{\mathrm{opt}})=\sum_k P^{\mathrm{opt}}(S\in C_k)P\left(S|\boldsymbol{\mu}_k^{\mathrm{opt}},\boldsymbol{\Sigma}_k^{\mathrm{opt}}\right) \tag{9}$$

where $\boldsymbol{\Theta}^{\mathrm{opt}}=\left\{\boldsymbol{\mu}_k^{\mathrm{opt}},\boldsymbol{\Sigma}_k^{\mathrm{opt}},P\left(\boldsymbol{s}_j\in C_k^{\mathrm{opt}}\right)\right\}$ is the optimal parameter set. The illustration of the GMM is given in Fig. 3, and the solution of $\boldsymbol{\Theta}^{\mathrm{opt}}$ will be elaborated in Section 3.

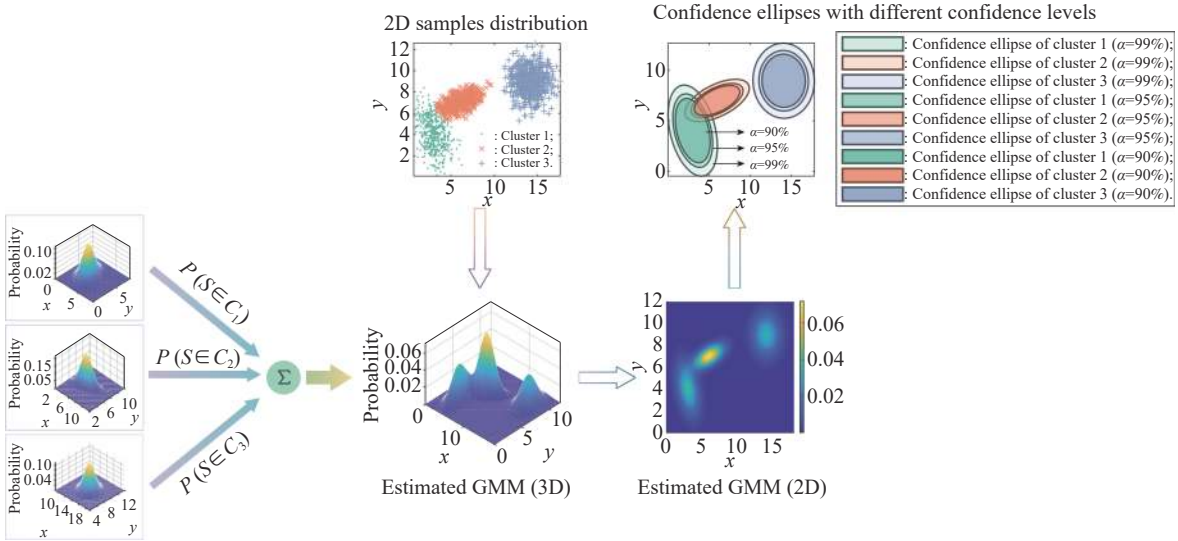

Fig. 3 Illustration of GMM, classification, and confidence area

In this paper, the confidence ellipse is applied to depict the confidence area, as shown in Fig. 3. The function of confidence ellipse can be expressed as

$$\frac{x^2}{\lambda_{k,1}}+\frac{y^2}{\lambda_{k,2}}=s_0 \tag{10}$$

where x and y are the samples in the range and azimuth directions. In this paper, the value of s_0 is 5.991 corresponding to the 95% confidence level α.

The values of $\lambda_{k,1}$ and $\lambda_{k,2}$ can be obtained by the principal component analysis:

$$\begin{cases}\boldsymbol{\Sigma}_k^{\mathrm{opt}}\boldsymbol{V}=\boldsymbol{V}\boldsymbol{D}\\ \boldsymbol{D}=\begin{bmatrix}\lambda_{k,1}&0\\0&\lambda_{k,2}\end{bmatrix}\end{cases} \tag{11}$$

where $\boldsymbol{V}$ is the eigenmatrix, which shows the directions of major and minor axes, and the lengths of major axis and minor axis are as follows:

$$2a_k=2\sqrt{s_0\lambda_{k,1}}, \tag{12}$$

$$2b_k=2\sqrt{s_0\lambda_{k,2}}. \tag{13}$$

Then, the confidence ellipse of the kth Gaussian distribution can be expressed as follows:

$$\begin{bmatrix} x \\ y \end{bmatrix} = \boldsymbol{V}\begin{bmatrix} a_k\cos\phi \\ b_k\sin\phi \end{bmatrix} + \boldsymbol{\mu}_k^{\text{opt}},\ \phi\in[-\pi,\pi]. \tag{14}$$

3. A method for extracting ship target with overlaps in SAR image via EM algorithm

In this section, a novel method for extracting the ship target with overlaps is proposed, which involves the EM algorithm and the amplitude estimation method. Firstly, the principle of the proposed method is introduced. Then, the main steps of the proposed method are given. The proposed method can achieve the target separation and IPP extraction. Consequently, the image quality can be improved, the image resolution can be ensured, and the more complete target can be obtained.

3.1 Principle of the proposed method

Primarily, the clustering analysis technique is implemented. For calculating the posterior probability in (7), a group of optimal parameters should be acquired, denoted as $\boldsymbol{\Theta}^{\text{opt}}=\left\{\left(\boldsymbol{\mu}_k^{\text{opt}},\boldsymbol{\Sigma}_k^{\text{opt}},P\left(\boldsymbol{s}_j\in C_k^{\text{opt}}\right)\right),k=1,2,\cdots,K\right\}$. In this paper, the EM algorithm is adopted to solve this issue, and the main steps are as follows. First, with the initial parameter of $\boldsymbol{\Theta}^{(0)}$, the posterior probability of $P^{(1)}(\boldsymbol{s}_j\in C_k|\boldsymbol{s}_j;\boldsymbol{\Theta}^{(0)})$ is calculated via (7). Second, the position, intra-class error and posterior probability of each sample are used to update $\boldsymbol{\Theta}^{(1)}$ via the weighted average. The aforementioned two steps are named as E-step and M-step, which are repeated until the precision is satisfied. Finally, the optimal parameter of $\boldsymbol{\Theta}^{\text{opt}}$ and the classification result of $P^{\text{opt}}(\boldsymbol{s}_j\in C_k|\boldsymbol{s}_j)$ can be obtained.

Afterwards, an image amplitude estimation method is proposed to generate the radar image with the single IPP and single target, which ensures the completeness of the target. The illustration of amplitude estimation is shown in Fig. 4. It is considered that the image amplitude of $I(\boldsymbol{s}_j)$ consists of the image amplitudes of multiple clusters, which can be expressed as

$$I(\boldsymbol{s}_j)=\sum_k I_k(\boldsymbol{s}_j) \tag{15}$$

where $I_k(\boldsymbol{s}_j)$ is the image amplitude with $\boldsymbol{s}_j\in C_k$.

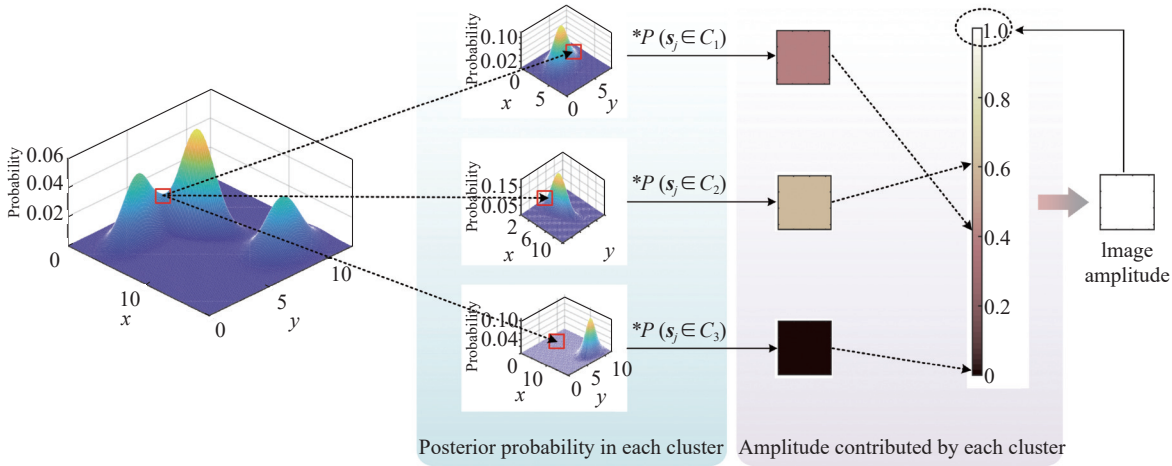

Fig. 4 Illustration of amplitude estimation

It is observed that the posterior probability of $P^{\text{opt}}(\boldsymbol{s}_j\in C_k|\boldsymbol{s}_j)$ can depict the possibility that $\boldsymbol{s}_j$ belongs to C_k. Hence, the image amplitude of $I_k(\boldsymbol{s}_j)$ can be estimated by

$$I_k(\boldsymbol{s}_j)=P^{\text{opt}}(\boldsymbol{s}_j\in C_k|\boldsymbol{s}_j)I(\boldsymbol{s}_j). \tag{16}$$

Based on (16), the K radar images with single IPP and single target can be obtained as $I_1(S),I_2(S),\cdots,I_K(S)$.

In (16), when $\boldsymbol{s}_j$ hardly belongs to C_k, the value of $I_k(\boldsymbol{s}_j)$ will be small. When $\boldsymbol{s}_j$ almost belongs to C_k, the value of $I_k(\boldsymbol{s}_j)$ will be large. Hence, the kth radar image of $I_k(S)$ only contains the kth IPP or the kth target, while other IPPs or targets cannot be presented.

Another advantage of the amplitude estimation with (16) is that the more target information can be retained. Without the amplitude estimation, the overlapping pixels will be lost, and the ship target in the SAR image will be incomplete. A simple example is used for illustration. We assume that $\boldsymbol{s}_j$ is an overlapping sample in the SAR image. The probabilities of $\boldsymbol{s}_j\in C_1$ and $\boldsymbol{s}_j\in C_2$ are denoted as $P^{\text{opt}}(\boldsymbol{s}_j\in C_1|\boldsymbol{s}_j)$ and $P^{\text{opt}}(\boldsymbol{s}_j\in C_2|\boldsymbol{s}_j)$, respectively. It can be predicted that $P^{\text{opt}}(\boldsymbol{s}_j\in C_1|\boldsymbol{s}_j)$ will be similar to $P^{\text{opt}}(\boldsymbol{s}_j\in C_2|\boldsymbol{s}_j)$. Hence, the amplitudes of $I_1(\boldsymbol{s}_j)$ and $I_2(\boldsymbol{s}_j)$ are close.

Without the amplitude estimation, the sample of $\boldsymbol{s}_j$ is

only classified as a single cluster, assumed as $\boldsymbol{s}_j \in C_1$. The amplitudes of $\boldsymbol{s}_j$ in the first and second radar images are estimated as $I_1(\boldsymbol{s}_j) = I(\boldsymbol{s}_j)$ and $I_2(\boldsymbol{s}_j) = 0$, respectively. Apparently, the overlapping pixels will appear in the first radar image, and their intensities will be higher than other pixels. Furthermore, the second radar image will miss these overlapping pixels, and the ship target will be incomplete. Therefore, estimating image amplitude is important for ensuring the completeness of ship target in the radar image.

With the proposed method, the amplitudes of overlapping pixel $\boldsymbol{s}_j$ in the first and second radar images can be estimated as $I_1(\boldsymbol{s}_j) = P^{\text{opt}}(\boldsymbol{s}_j \in C_1|\boldsymbol{s}_j) I(\boldsymbol{s}_j)$ and $I_2(\boldsymbol{s}_j) = P^{\text{opt}}(\boldsymbol{s}_j \in C_2|\boldsymbol{s}_j) I(\boldsymbol{s}_j)$, respectively. The overlapping pixels will appear both in the first and second radar images, which ensures the completeness of the ship target.

3.2 Procedure of the proposed method

The flowchart of the proposed method is shown in Fig. 5.

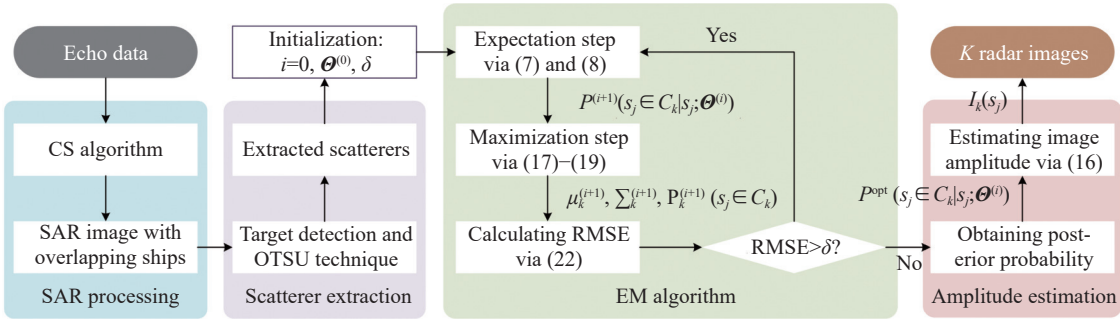

Fig. 5 Flowchart of the proposed method

The main steps are as follows:

Step 1 Obtain the SAR image, and establish the sample set via the data preprocessing technique.

Step 2 Initialize $i = 0$, set a group of initial parameters $\boldsymbol{\Theta}^{(0)}$, and determine the precision as δ.

Step 3 Accomplish the E-step via (7) and (8). The new posterior probability can be denoted as $P^{(i+1)}(\boldsymbol{s}_j \in C_k|\boldsymbol{s}_j;\boldsymbol{\Theta}^{(i)})$, where $j = 1,2,\cdots,J$, $k = 1,2,\cdots,K$.

Step 4 Implement the M-step via (17)−(19).

$$\boldsymbol{\mu}_k^{(i+1)} = \frac{\sum_j \boldsymbol{s}_j P^{(i+1)}\left(\boldsymbol{s}_j \in C_k|\boldsymbol{s}_j;\boldsymbol{\Theta}^{(i)}\right)}{\sum_j P^{(i+1)}\left(\boldsymbol{s}_j \in C_k|\boldsymbol{s}_j;\boldsymbol{\Theta}^{(i)}\right)}, \tag{17}$$

$$\boldsymbol{\Sigma}_k^{(i+1)} = \frac{\sum_j \left(\boldsymbol{s}_j - \boldsymbol{\mu}_k^{(i+1)}\right)\left(\boldsymbol{s}_j - \boldsymbol{\mu}_k^{(i+1)}\right)^{\mathrm{T}} P^{(i+1)}\left(\boldsymbol{s}_j \in C_k|\boldsymbol{s}_j;\boldsymbol{\Theta}^{(i)}\right)}{\sum_j P^{(i+1)}\left(\boldsymbol{s}_j \in C_k|\boldsymbol{s}_j;\boldsymbol{\Theta}^{(i)}\right)}, \tag{18}$$

$$P^{(i+1)}(\boldsymbol{s}_j \in C_k) = \frac{1}{J}\sum_j P^{(i+1)}\left(\boldsymbol{s}_j \in C_k|\boldsymbol{s}_j;\boldsymbol{\Theta}^{(i)}\right). \tag{19}$$

Step 5 Compare the root mean square error $\text{RMSE}(\boldsymbol{\Theta}^{(i)}, \boldsymbol{\Theta}^{(i+1)})$ with the precision of δ.

If $\text{RMSE}(\boldsymbol{\Theta}^{(i)}, \boldsymbol{\Theta}^{(i+1)}) \leqslant \delta$, we can obtain the classification results as follows:

$$P^{\text{opt}}(\boldsymbol{s}_j \in C_k|\boldsymbol{s}_j) = P^{(i+1)}\left(\boldsymbol{s}_j \in C_k|\boldsymbol{s}_j;\boldsymbol{\Theta}^{(i)}\right), \tag{20}$$

$$\boldsymbol{\Theta}^{\text{opt}} = \boldsymbol{\Theta}^{(i+1)}. \tag{21}$$

Then, Step 6 is implemented.

Otherwise, the iteration number is updated as $i = i + 1$, and Step 3−Step 5 are repeated.

Here, $\text{RMSE}(\boldsymbol{\Theta}^{(i)}, \boldsymbol{\Theta}^{(i+1)})$ is calculated by

$$\text{RMSE}\left(\boldsymbol{\Theta}^{(i)}, \boldsymbol{\Theta}^{(i+1)}\right) = \frac{\sum_k \left(\boldsymbol{\mu}_k^{(i+1)} - \boldsymbol{\mu}_k^{(i)}\right)^{\mathrm{T}}\left(\boldsymbol{\mu}_k^{(i+1)} - \boldsymbol{\mu}_k^{(i)}\right)}{DK} + \frac{\sum_k \sum_s \sum_r \left(\sigma_{k,rs}^{(i+1)} - \sigma_{k,rs}^{(i)}\right)^2}{D^2 K} + \frac{\sum_k \left(P^{(i+1)}(\boldsymbol{s}_j \in C_k) - P^{(i)}(\boldsymbol{s}_j \in C_k)\right)^2}{K} \tag{22}$$

where $\sigma_{k,rs}^{(i)}$ is the element of $\boldsymbol{\Sigma}_k^{(i)}$ in the rth row and the sth column, and $r, s = 1,2$.

Step 6 Estimate the amplitude with (16), and generate the K radar images of $I_1(S), I_2(S), \cdots, I_K(S)$.

Remark 1 The recognition system can be applied to distinguish whether the special case exists. The radar images with the proposed method are input to the recognition system. With the given recognition threshold, if the target can be successfully recognized, the value of K can be determined. The value of K starts with 1 and increases gradually.

Remark 2 Additionally, the recognition system can distinguish which kind of special case appears. If the recognition result shows single target, the case of multiple IPPs will happen. If the recognition result shows mul-

tiple target types, the case of overlapping targets will exist.

4. Experiment results

In this section, the *k*-means algorithm and EM algorithm are employed to extract the single IPP and single target for comparison with the proposed method.

4.1 Simulated data in the case of multiple IPPs

The parameters of the simulated data are listed in Table 1, and the scatterer model is shown in Fig. 6. The ship target has 3D sinusoidal rotation (roll, pitch, and yaw), the rotation amplitudes are 1.80, 0.21, and 0.24 degrees, respectively, and the rotation periods are 16.2 s, 28.3 s, and 13.3 s, respectively. The CS algorithm in [28] is adopted for the SAR imaging. Obviously, there are multiple IPPs in the SAR image, as shown in Fig. 7, which degrades the image quality.

Table 1 Parameters of simulated data

Parameter	Value
Sample frequency/MHz	200
Bandwidth/MHz	60
Pulse repetition frequency/MHz	200
Pulse width/μs	10
Carrier frequency/GHz	5.3
Aircraft height/km	10
Aircraft velocity/(m/s)	50

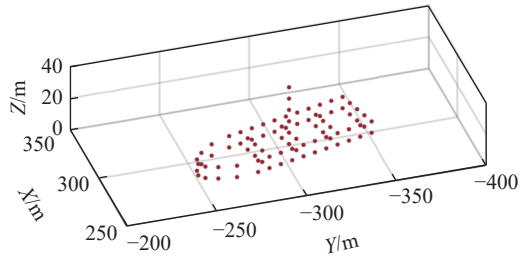

Fig. 6 Scatterer model of ship target in the case of multiple IPPs

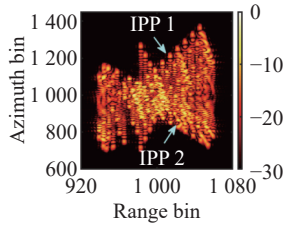

Fig. 7 SAR image of ship target with multiple IPPs for simulated data

Afterwards, the data preprocessing technique is employed for better extracting the scatterers of ship target. The processing results are summarized in Fig. 8(a)–Fig. 8(h). First, the potential samples are selected by the prescreening technique, as shown in Fig. 8(a). Then, the morphological filtering technique is applied to remove the isolated samples, as shown in Fig. 8(b). The samples neighboring in the 4-connectivity area are labeled, with which the 2D sample sets are generated. The labeled sample sets and their centres are demonstrated in Fig. 8(c) and Fig. 8(d), respectively. Afterwards, some sample sets with the low intensity and small size are eliminated via the rejection technique, as shown in Fig. 8(e). Moreover, the sample sets of the same ship target are merged via the fusion technique, as shown in Fig. 8(f). The change of sample set number is demonstrated in Fig. 8(g) from the steps of morphological filtering, rejection and fusion. However, some high-sidelobe samples are still remained, which are eliminated by the OTSU method, as shown in Fig. 8(h). Subsequently, the scatterers are extracted, as shown in Fig. 9.

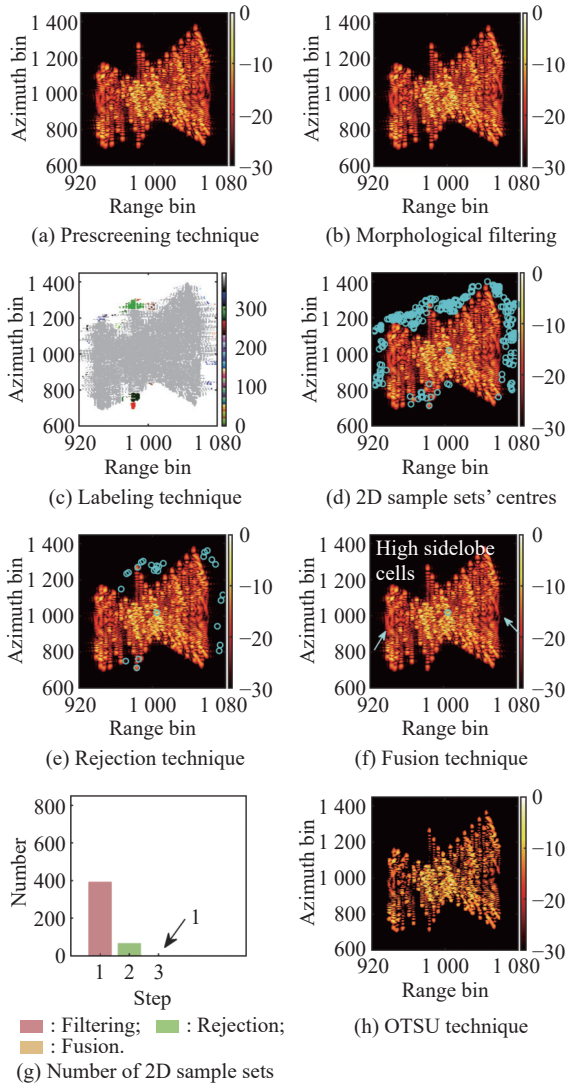

Fig. 8 SAR image with multiple IPPs after data preprocessing for simulated data

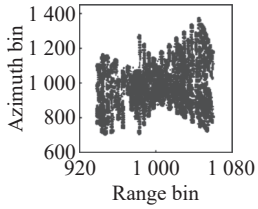

Fig. 9 Extraction results of scatterers in SAR image with multiple IPPs for simulated data

Different clustering algorithms are adopted to classify the scatterers in Fig. 9. The results of different clustering algorithms are shown in Fig. 10. The green and orange shadow areas represent the confidence ellipses of the first and second clusters, respectively. Apparently, the *k*-means method cannot classify the scatterers of two IPPs correctly, as shown in Fig. 10(a), whereas the scatterers of two IPPs are extracted accurately via the EM algorithm, as shown in Fig. 10(b). Hence, the EM algorithm has superior performance for the classification of overlapping scatterers.

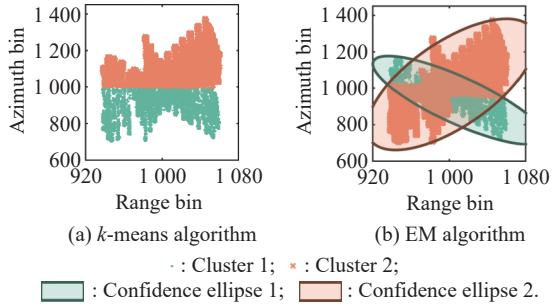

Fig. 10 Results of different clustering algorithms in the case of multiple IPPs for simulated data

The parameters of the EM algorithm and confidence ellipse are listed in Table 2, including the mean and covariance matrix of each cluster, the eigenvalues and eigenvectors of the covariance matrix, and the lengths of the major and minor axis for the confidence ellipse. Here, the confidence level is determined as 95%.

Table 2 Parameters of EM algorithm and confidence ellipse for simulated data in the case of multiple IPPs

Cluster	$\boldsymbol{\mu}_k^{\text{opt}}$	$\boldsymbol{\Sigma}_k^{\text{opt}}$	Eigenvalue		Axis length of ellipse		Eigenvector	
			$\lambda_{k,1}$	$\lambda_{k,2}$	a_k	b_k	$\boldsymbol{v}_{k,1}$	$\boldsymbol{v}_{k,2}$
1	$[\,1\,009.5 \quad 933.9\,]^{\mathrm{T}}$	$\begin{bmatrix} 1\,341.5 & -2\,971.3 \\ -2\,971.3 & 9\,830.2 \end{bmatrix}$	405.0	10 767.0	49.25	253.98	$[\,-0.95 \quad -0.30\,]^{\mathrm{T}}$	$[\,-0.30 \quad 0.95\,]^{\mathrm{T}}$
2	$[\,1\,002.0 \quad 1\,021.0\,]^{\mathrm{T}}$	$\begin{bmatrix} 1\,300.0 & 3\,495.0 \\ 3\,495.0 & 2\,162.1 \end{bmatrix}$	716.0	22 205.0	65.50	364.73	$[\,-0.99 \quad 0.16\,]^{\mathrm{T}}$	$[\,0.16 \quad 0.99\,]^{\mathrm{T}}$

The extraction results of the *k*-means algorithm are shown in Fig. 11, where Fig. 11(a) and Fig. 11(b) are the first and second extraction results, respectively. Obviously, the radar images in Fig. 11 cannot present the entire ship target, since the *k*-means algorithm classifies the scatterers of the ship target incorrectly.

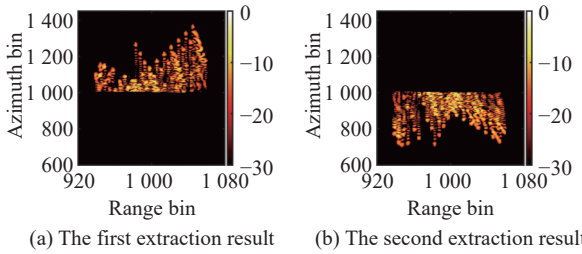

Fig. 11 Extraction results of two IPPs via *k*-means algorithm for simulated data

The extraction results of the EM algorithm are shown in Fig. 12, where Fig. 12(a) and Fig. 12(b) are the first and second extraction results, respectively. Compared with the *k*-means algorithm, the ship targets in Fig. 12 are more complete owing to the well classification, but some overlapping pixels are lost.

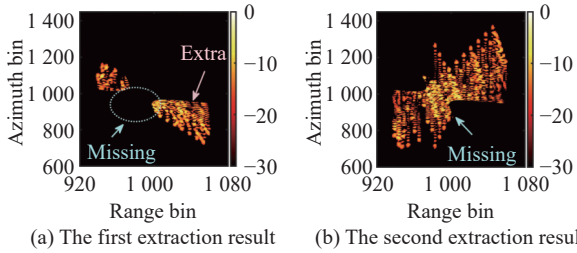

Fig. 12 Extraction results of two IPPs via EM algorithm for simulated data

The extraction results of the proposed method are demonstrated in Fig. 13(a) and Fig. 13(b), respectively. Overlapping pixels appear simultaneously in Fig. 13(a) and Fig. 13(b). Moreover, the image quality is improved compared with Fig. 8.

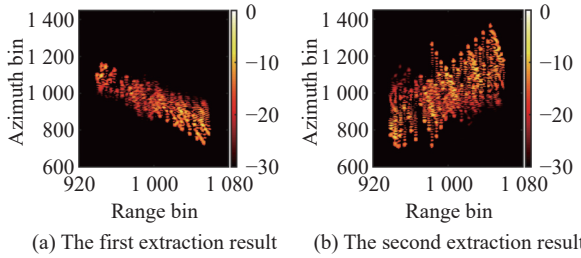

Fig. 13 Extraction results of two IPPs via the proposed method for simulated data

Hence, the proposed method can improve the image quality, ensure the imaging resolution, and reserve the completeness of the ship target.

4.2 Simulated data in the case of overlapping targets

The parameters of the radar system are listed in Table 1. The scatterer models of two ship targets are shown in Fig. 14. Obviously, two ship targets are overlapped in the SAR image in Fig. 15, as shown in the area with the dotted line. The SAR image is preprocessed for better extracting the scatterers of the ship target, and the extracted scatterers are shown in Fig. 16.

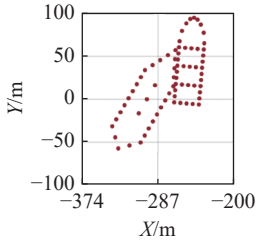

Fig. 14 Scatterer model of ship target in the case of multiple overlapping targets

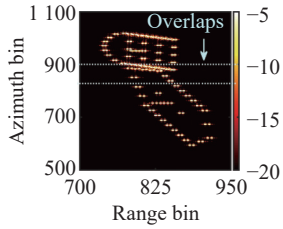

Fig. 15 SAR image of multiple ship targets with overlaps for simulated data

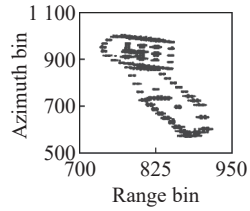

Fig. 16 Extraction results of scatterers in SAR image with overlapping targets for simulated data

Afterwards, the clustering results of the k-means algorithm and the EM algorithm are shown in Fig. 17(a) and Fig. 17(b), respectively, both of which have the similar performance. The parameters of the EM algorithm and the confidence ellipse are listed in Table 3. The extraction results of the k-means algorithm are exhibited in Fig. 18(a) and Fig. 18(b). The redundant details of the second ship target exist in Fig. 18(a), while the second ship target are incomplete in Fig. 18(b). The extraction results of the EM algorithm are displayed in Fig. 19(a) and Fig. 19(b), which shows the similar performance with the k-means algorithm.

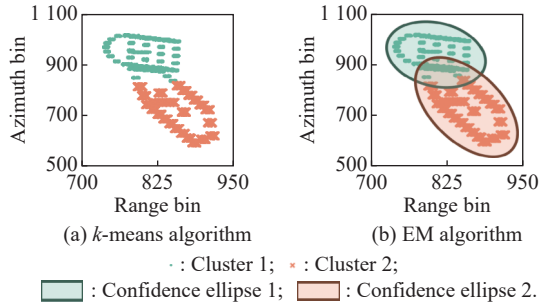

Fig. 17 Results of different clustering algorithms in the case of multiple overlapping targets for simulated data

Table 3 Parameters of EM algorithm and confidence ellipse for simulated data in the case of multiple overlapping targets

Cluster	$\boldsymbol{\mu}_k^{\text{opt}}$	$\boldsymbol{\Sigma}_k^{\text{opt}}$	Eigenvalue ($\times 10^3$)		Axis length of ellipse		Eigenvector	
			$\lambda_{k,1}$	$\lambda_{k,2}$	a_k	b_k	$\boldsymbol{v}_{k,1}$	$\boldsymbol{v}_{k,2}$
1	$[\,805.38 \quad 940.40\,]^{\mathrm{T}}$	$\begin{bmatrix} 1\,094.4 & -369.1 \\ -369.1 & 2\,834.9 \end{bmatrix}$	1.02	2.91	78.15	132.04	$[\,-0.98 \quad -0.20\,]^{\mathrm{T}}$	$[\,0.20 \quad -0.98\,]^{\mathrm{T}}$
2	$[\,855.23 \quad 732.14\,]^{\mathrm{T}}$	$\begin{bmatrix} 1\,175.9 & -1\,448.4 \\ -1\,448.4 & 6\,463.2 \end{bmatrix}$	0.81	6.83	69.45	202.34	$[\,-0.97 \quad -0.25\,]^{\mathrm{T}}$	$[\,-0.25 \quad 0.97\,]^{\mathrm{T}}$

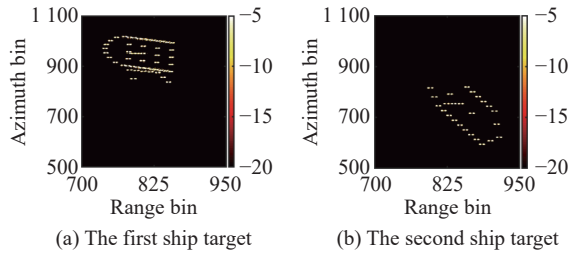

Fig. 18 Extraction results of ship targets via k-means algorithm in the case of multiple overlapping targets for simulated data

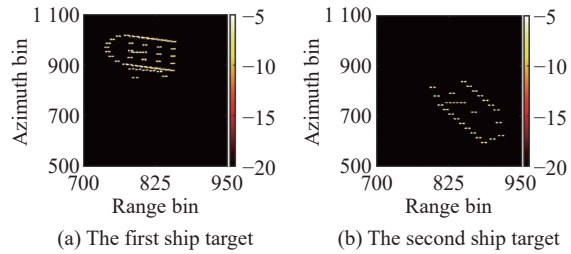

Fig. 19 Extraction results of ship targets via EM algorithm in the case of multiple overlapping targets for simulated data

The extraction results of the proposed method are demonstrated in Fig. 20(a) and Fig. 20(b), respectively. Compared with Fig. 18 and Fig. 19, the radar image in Fig. 20(a) shows the lower amplitudes of the second ship target, meanwhile the more details of the second ship body are shown in Fig. 20(b). Hence, the proposed method shows better performance.

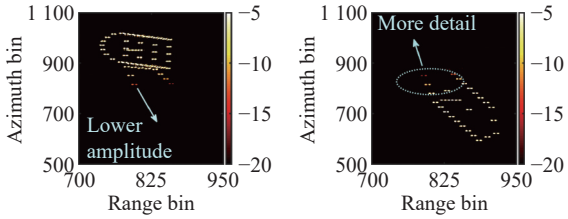

Fig. 20 Extraction results of ship targets via the proposed method in the case of multiple overlapping targets for simulated data

4.3 Real measured data in the case of multiple IPPs

The parameters of real measured data are listed in Table 4. The SAR imaging result of the multiple IPPs is shown in Fig. 21. Obviously, the complex motion of the ship target induces multiple IPPs.

Table 4 Parameters of real measured data

Parameter	Value
Sample frequency/MHz	100
Bandwidth/MHz	60
Pulse repetition frequency/Hz	500
Pulse width/μs	10
Carrier frequency	C band
Range center/km	4.175
Aircraft velocity/(m/s)	50

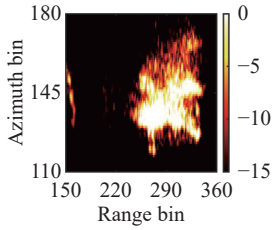

Fig. 21 SAR image of ship target with multiple IPPs for real measured data

The SAR imaging results after the data preprocessing are sketched in Fig. 22(a)–Fig. 22(h). Primarily, the potential samples of ship target are selected, as given in Fig. 22(a). Then, some isolated samples are removed by the morphological filter, as shown in Fig. 22(b). Afterwards, the connected samples are labeled and the sample sets are generated, as displayed in Fig. 22(c). The centres of sample sets are marked in Fig. 22(d). Moreover, the sample sets with the small size and low intensity are eliminated, as shown in Fig. 22(e). The sample sets of the same ship target are merged, as demonstrated in Fig. 22(f). The change of sample set numbers is shown in Fig. 22(g). Finally, the samples with the high sidelobe are removed via the OTSU method, as shown in Fig. 22(h).

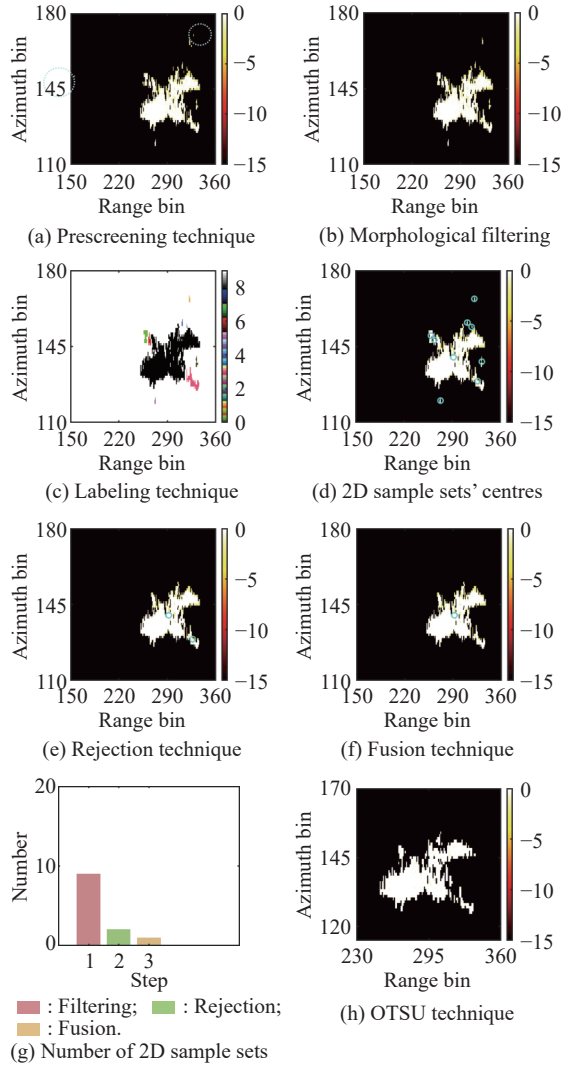

Fig. 22 SAR image after data preprocessing in the case of multiple IPPs for real measured data

Then, the scatterers of the ship target are extracted, as shown in Fig. 23, which are classified by the *k*-means and EM algorithms. The cluster result of the *k*-means algorithm is shown in Fig. 24(a), in which the scatterers cannot be classified correctly based on the IPP. The cluster result of the EM algorithm is given in Fig. 24(b), in which the scatterers are classified accurately. The param-

eters of EM algorithm and confidence ellipse are listed in Table 5.

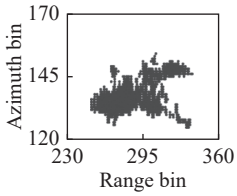

Fig. 23 Extraction results of scatterers in the SAR image with multiple IPPs for real measured data

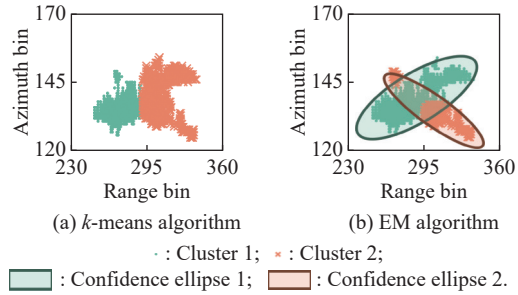

Fig. 24 Results of different clustering algorithms in the case of multiple IPPs for real measured data

Table 5 Parameters of EM algorithm and confidence ellipse for real measured data in the case of multiple IPPs

Cluster	$\boldsymbol{\mu}_k^{\text{opt}}$	$\boldsymbol{\Sigma}_k^{\text{opt}}$	Eigenvalue ($\times 10^3$)		Axis length of ellipse		Eigenvector	
			$\lambda_{k,1}$	$\lambda_{k,2}$	a_k	b_k	$\boldsymbol{v}_{k,1}$	$\boldsymbol{v}_{k,2}$
1	$[\ 288.50 \quad 139.44\ ]^{\mathrm{T}}$	$\begin{bmatrix} 441.84 & 95.72 \\ 95.92 & 38.18 \end{bmatrix}$	16.63	463.39	9.98	52.69	$[\ 0.22 \quad -0.98\ ]^{\mathrm{T}}$	$[\ -0.98 \quad -0.22\ ]^{\mathrm{T}}$
2	$[\ 303.19 \quad 134.67\ ]^{\mathrm{T}}$	$\begin{bmatrix} 300.82 & -83.41 \\ -83.41 & 30.22 \end{bmatrix}$	6.58	324.47	6.28	44.09	$[\ -0.27 \quad -0.96\ ]^{\mathrm{T}}$	$[\ -0.96 \quad 0.27\ ]^{\mathrm{T}}$

The extraction results of two IPPs via the k-means algorithm are demonstrated in Fig. 25(a) and Fig. 25(b). Apparently, the ship targets in Fig. 25(a) and Fig. 25(b) are not complete.

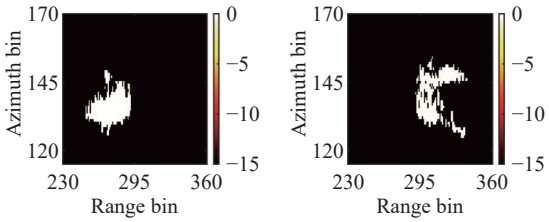

Fig. 25 Extraction results of two IPPs via k-means algorithm for real measured data

The extraction results of two IPPs via the EM algorithm are displayed in Fig. 26(a) and Fig. 26(b). Obviously, the radar images in Fig. 26 miss some details of ship body without the amplitude estimation.

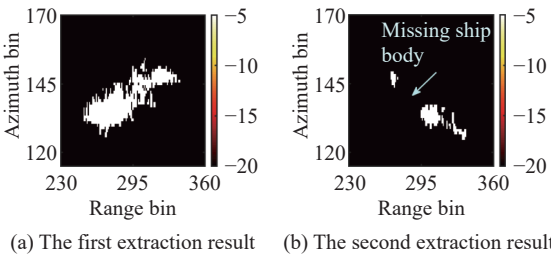

Fig. 26 Extraction results of two IPPs via EM algorithm for real measured data

The extraction results of the proposed method are shown in Fig. 27(a) and Fig. 27(b). Compared with Fig. 26, the overlapping pixels are shown simultaneously in Fig. 27(a) and Fig. 27(b). Hence, the proposed method can recover more details of the ship body.

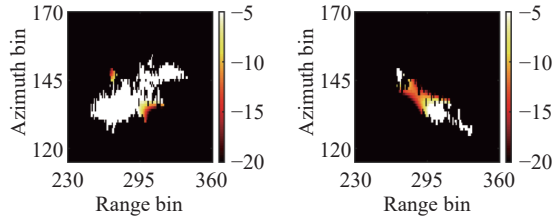

Fig. 27 Extraction results of two IPPs via the proposed method for real measured data

4.4 Real measured data in the case of overlapping targets

The parameters of real measured data are listed in Table 4. The SAR image is shown in Fig. 28, where the ship targets are overlapping in the range and azimuth directions. Then, the scatterers of ship targets are extracted, as shown in Fig. 29, which are classified by the k-means algorithm and the EM algorithm.

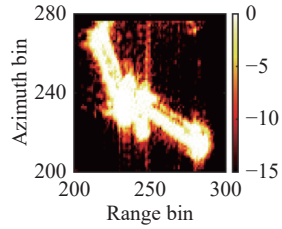

Fig. 28 SAR image of multiple ship targets with overlaps for real measured data

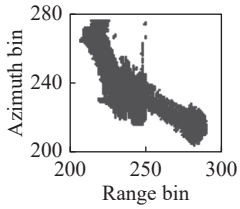

Fig. 29 Extraction results of scatterers in SAR image in the case of multiple overlapping targets with real measured data

The clustering result of *k*-means algorithm is shown in Fig. 30(a), in which the overlapping scatterers are not classified well. The clustering result of EM algorithm is given in Fig. 30(b), in which the scatterers of two targets are classified properly. The parameters of EM algorithm and confidence ellipse are listed in Table 6.

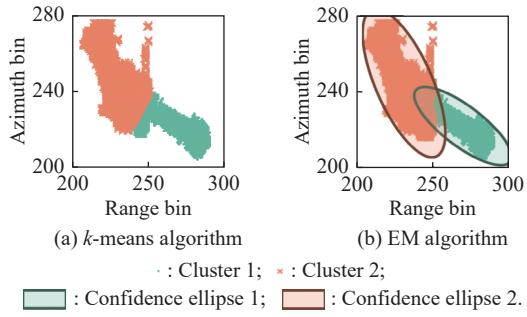

Fig. 30 Results of different clustering algorithms in the case of multiple overlapping targets with real measured data

Table 6 Parameters of EM algorithm and confidence ellipse for real measured data in the case of multiple overlapping targets

Cluster	$\boldsymbol{\mu}_k^{\text{opt}}$	$\boldsymbol{\Sigma}_k^{\text{opt}}$	Eigenvalue		Axis length of ellipse		Eigenvector	
			$\lambda_{k,1}$	$\lambda_{k,2}$	a_k	b_k	$\boldsymbol{v}_{k,1}$	$\boldsymbol{v}_{k,2}$
1	$[\,269.58 \quad 221.96\,]^{\mathrm{T}}$	$\begin{bmatrix} 170.56 & -85.78 \\ -85.78 & 70.31 \end{bmatrix}$	21.09	219.78	11.24	36.29	$[\,-0.50 \quad -0.87\,]^{\mathrm{T}}$	$[\,0.87 \quad -0.50\,]^{\mathrm{T}}$
2	$[\,230.86 \quad 244.46\,]^{\mathrm{T}}$	$\begin{bmatrix} 123.95 & -119.26 \\ -119.26 & 252.49 \end{bmatrix}$	52.74	323.70	17.78	44.04	$[\,-0.86 \quad -0.51\,]^{\mathrm{T}}$	$[\,-0.51 \quad 0.86\,]^{\mathrm{T}}$

The extraction results of two ship targets via the *k*-means algorithm are shown in Fig. 31(a) and Fig. 31(b), respectively. Obviously, the extra detail of the second ship target exists in Fig. 31(a), and the body of the second ship target is incomplete in Fig. 31(b).

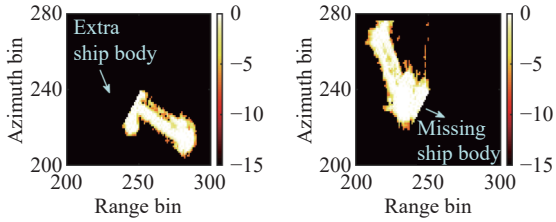

Fig. 31 Extraction results of overlapping ship targets via *k*-means algorithm for real measured data

The extraction results of two ship targets via the EM algorithm are displayed in Fig. 32(a) and Fig. 32(b). Visibly, the performance is better than the *k*-means algorithm, whereas some overlapping pixels are lost.

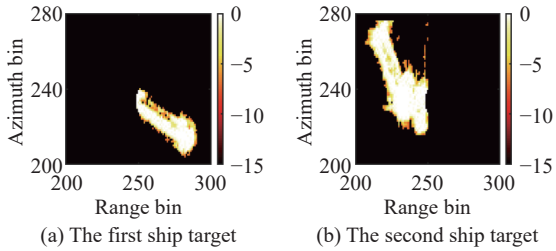

Fig. 32 Extraction results of overlapping ship targets via EM algorithm for real measured data

The extraction results of the proposed method are demonstrated in Fig. 33(a) and Fig. 33(b). Compared with Fig. 32, the more details of the ship target are depicted in Fig. 33 after the amplitude estimation. Therefore, the proposed method has the superior performance.

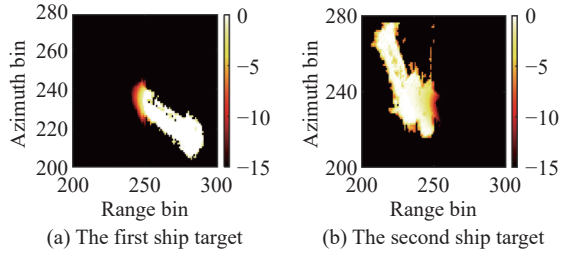

Fig. 33 Extraction results of overlapping ship targets via the proposed method for real measured data

5. Conclusions

This paper achieves the IPP selection and target separation for the ship target with overlaps in the SAR image. It is found that the overlapping pixels belong to the multiple clusters with certain probabilities, which can be estimated via the clustering analysis. Given above, a novel method for extracting the ship target with overlaps is proposed in this paper. Three main steps are composed as follows. First, the scatterers of the ship target are well extracted with the data preprocessing technique. Then, the EM algorithm is adopted for the IPP selection and target separation, because it has the superior performance for classifying the overlapping pixels. Afterwards, a

novel amplitude estimation approach is proposed, which utilizes the posterior probability generated by the EM algorithm adequately. The proposed method can reserve the more target information, ensure the image resolution and improve the image quality simultaneously. Results of simulated and real measured data verify the effectiveness of the proposed method.

References

[1] LI N, XING M D, HOU Y X, et al. Ship focusing and positioning based on 2D ambiguity resolving for single-channel SAR mounted on high-speed maneuvering platforms with small aperture. IEEE Trans. on Geoscience and Remote Sensing, 2022, 60: 5221213.

[2] WANG X Q, LI G, PLAZA A, et al. Ship detection in SAR images by aggregating densities of Fisher vectors: extension to a global perspective. IEEE Trans. on Geoscience and Remote Sensing, 2022, 60: 2506613.

[3] ZHANG T Y, LIU S J, DING Z G, et al. A motion state judgment and radar imaging algorithm selection method for ship. IEEE Trans. on Geoscience and Remote Sensing, 2022, 60: 5236318.

[4] ZHANG J Q, WANG Y, LU X F. Distributed inverse synthetic aperture radar imaging of ship target with complex motion. Journal of Systems Engineering and Electronics, 2021, 32(6): 1325–1337.

[5] CHEN S Y, WANG Y, CAO R. A high frequency vibration compensation approach for ultra-high resolution SAR imaging based on sinusoidal frequency modulation Fourier-Bessel transform. Journal of Systems Engineering and Electronics, 2023, 34(4): 894–905.

[6] HUANG P H, XIA X G, ZHAN M Y, et al. ISAR imaging of a maneuvering target based on parameter estimation of multicomponent cubic phase signals. IEEE Trans. on Geoscience and Remote Sensing, 2022, 60: 5103918.

[7] MARTORELLA M, PASTINA D, BERIZZI F, et al. Spaceborne radar imaging of maritime moving targets with the Cosmo-SkyMed SAR system. IEEE Journal of Selected Topics in Applied Earth Observations and Remote Sensing, 2014, 7(7): 2797–2810.

[8] SHAO S, LIU H W, ZHANG L, et al. Integration of super-resolution ISAR imaging and fine motion compensation for complex maneuvering ship targets under high sea state. IEEE Trans. on Geoscience and Remote Sensing, 2022, 60: 5222820.

[9] MARTORELLA M. Optimal sensor positioning for inverse synthetic aperture radar. IEEE Trans. on Aerospace and Electronic Systems, 2013, 49(1): 648–658.

[10] CHEN Y M, ZHOU P, DAI Y S. Application of an existing approach to refocusing maritime moving targets on Radarsat-2 SLC images. Proc. of the IEEE 5th Asia-Pacific Conference on Synthetic Aperture Radar, 2015: 502−506.

[11] SHAO S, ZHANG L, LIU H W. An optimal imaging time interval selection technique for marine targets ISAR imaging based on sea dynamic prior information. IEEE Sensors Journal, 2019, 19(13): 4940–4953.

[12] PASTINA D, MONTANARI A, APRILE A. Motion estimation and optimum time selection for ship ISAR imaging. Proc. of the IEEE Radar Conference, 2003: 7−14.

[13] PASTINA D, SPINA C, APRILE A. A slope-based technique for motion estimation and optimum time selection for ISAR imaging of ship targets. Proc. of the 14th European Signal Processing Conference, 2006: 1−5.

[14] LI N, SHEN Q Y, WANG L, et al. Optimal time selection for ISAR imaging of ship targets based on time-frequency analysis of multiple scatterers. IEEE Geoscience and Remote Sensing Letters, 2022, 19: 4017505.

[15] CAO R, WANG Y, YEH C M, et al. A novel optimal time window determination approach for ISAR imaging of ship targets. IEEE Journal of Selected Topics in Applied Earth Observations and Remote Sensing, 2022, 15: 3475–3503.

[16] ZHOU P, ZHANG X, SUN W F, et al. Time-frequency analysis-based time-windowing algorithm for the inverse synthetic aperture radar imaging of ships. Journal of Applied Remote Sensing, 2018, 12(1): 1–20.

[17] LI N, WANG L, ZHU D Y. Optimal ISAR imaging time selection of ship targets using real data. Proc. of the IET International Radar Conference, 2013. DOI: 10.1049/cp.20130166.

[18] ZHOU P, ZHANG X, DAI Y S, et al. Time window selection algorithm for ISAR ship imaging based on instantaneous Doppler frequency estimations of multiple scatterers. IEEE Journal of Selected Topics in Applied Earth Observations and Remote Sensing, 2019, 12(10): 3799–3812.

[19] GAO F, HUO Y Y, WANG J, et al. Anchor-free SAR ship instance segmentation with centroid-distance based loss. IEEE Journal of Selected Topics in Applied Earth Observations and Remote Sensing, 2021, 14: 11352–11371.

[20] PASTINA F, FICO F, LOMBARDO P. Detection of ship targets in COSMO-SkyMed SAR images. Proc. of the IEEE Radar Conference, 2011: 928−933.

[21] OTSU N. A threshold selection method from gray-level histograms. IEEE Trans. on Systems, Man, and Cybernetics, 1979, 9(1): 62–66.

[22] ZHANG T W, ZHANG X L, SHI J, et al. Balance scene learning mechanism for offshore and inshore ship detection in SAR images. IEEE Geoscience and Remote Sensing Letters, 2022, 19: 4004905.

[23] LANG H T, XI Y Y, ZHANG X. Ship detection in high-resolution SAR images by clustering spatially enhanced pixel descriptor. IEEE Trans. on Geoscience and Remote Sensing, 2019, 57(8): 5407–5423.

[24] CAO R, WANG Y, ZHAO B, et al. Ship target imaging in airborne SAR system based on automatic image segmentation and ISAR technique. IEEE Journal of Selected Topics in Applied Earth Observations and Remote Sensing, 2021, 14: 1985–2000.

[25] KARAMI J, ALIMOHAMMADI A, MODABBERI S. Analysis of the spatio-temporal patterns of water pollution and source contribution using the MODIS sensor products and multivariate statistical techniques. IEEE Journal of Selected Topics in Applied Earth Observations and Remote Sensing, 2012, 5(4): 1243–1255.

[26] KIM G, YANG S, SIM J Y. Saliency-based initialisation of Gaussian mixture models for fully-automatic object segmentation. Electronics Letters, 2017, 53(25): 1648–1649.

[27] MCLACHLAN G J. The EM algorithm and extensions. Hoboken: Wiley, 2008.

[28] RANEY R K, RUNGE H, BAMLER R, et al. Precision SAR processing using chirp scaling. IEEE Trans. on Geoscience and Remote Sensing, 1994, 32(4): 786–799.

[29] ISA D, LEE L H, KALLIMANI V P, et al. Text document preprocessing with the Bayes formula for classification using the support vector machine. IEEE Trans. on Knowledge and Data Engineering, 2008, 20(9): 1264–1272.

Biographies

CAO Rui was born in 1996. She received her B.S. degree in electronic information engineering from Harbin Institute of Technology (HIT), Weihai, China, in 2018, and M.S. degree in information and communication engineering from HIT, Harbin, China, in 2020, where she is currently pursuing her Ph.D. degree in information and communication engineering. Her research interests include the field of radar imaging and radar signal processing.

E-mail: caor@hit.edu.cn

WANG Yong was born in 1979. He received his B.S. and M.S. degrees from Harbin Institute of Technology (HIT), Harbin, China, in 2002 and 2004, respectively, both in electronic engineering. He received his Ph.D. degree in information and communication engineering from HIT in 2008. He is currently a professor with the Institute of Electronic Engineering Technology in HIT. His main research interests are time frequency analysis of nonstationary signal, radar signal processing, and their application in synthetic aperture radar (SAR) imaging.

E-mail: wangyong6012@hit.edu.cn